# Noninvasive chorioretinal imaging in living rabbits using integrated photoacoustic microscopy and optical coherence tomography

CHAO TIAN,[1,2] WEI ZHANG,[2,3] AGHAPI MORDOVANAKIS,[2] XUEDING WANG,[2,4] AND YANNIS M. PAULUS[1,2,*]

[1]*Kellogg Eye Center, Department of Ophthalmology and Visual Sciences, University of Michigan, Ann Arbor, MI 48105, USA*

[2]*Department of Biomedical Engineering, University of Michigan, Ann Arbor, MI 48105, USA*

[3]*Institute of Biomedical Engineering, Chinese Academy of Medical Sciences & Peking Union Medical College, Tianjin 300192, China*

[4]*Department of Radiology, University of Michigan, Ann Arbor, MI 48105, USA*

* *ypaulus@med.umich.edu*

**Abstract:** Most reported photoacoustic ocular imaging work to date uses small animals, such as mice and rats, the eyeball sizes of which are less than one-third of those of humans, posing challenges for clinical translation. Here we developed a novel integrated photoacoustic microscopy (PAM) and optical coherence tomography (OCT) system for dual-modality chorioretinal imaging of larger animals, such as rabbits. The system has quantified lateral resolutions of 4.1 µm (PAM) and 3.8 µm (OCT), and axial resolutions of 37.0 µm (PAM) and 4.0 µm (OCT) at the focal plane of the objective. Experimental results in living rabbits demonstrate that the PAM can noninvasively visualize individual depth-resolved retinal and choroidal vessels using a laser exposure dose of ~80 nJ below the American National Standards Institute (ANSI) safety limit 160 nJ at 570 nm; and the OCT can finely distinguish different retinal layers, the choroid, and the sclera. This reported work may be a major step forward in clinical translation of the technology.

## References and links

1. D. Pascolini and S. P. Mariotti, "Global estimates of visual impairment: 2010," Br. J. Ophthalmol. **96**(5), 614–618 (2012).
2. P. A. Keane and S. R. Sadda, "Retinal imaging in the twenty-first century: state of the art and future directions," Ophthalmology **121**(12), 2489–2500 (2014).
3. A. Agarwal, *Fundus Fluorescein and Indocyanine Green Angiography: a Textbook and Atlas* (SLACK Incorporated, 2007).
4. P. A. Keane and S. R. Sadda, "Imaging chorioretinal vascular disease," Eye (Lond.) **24**(3), 422–427 (2010).
5. S. P. Mattison, W. Kim, J. Park, and B. E. Applegate, "Molecular imaging in optical coherence tomography," Curr. Mol. Imaging **3**(2), 88–105 (2014).
6. L. V. Wang and S. Hu, "Photoacoustic tomography: in vivo imaging from organelles to organs," Science **335**(6075), 1458–1462 (2012).
7. P. Beard, "Biomedical photoacoustic imaging," Interface Focus, rsfs20110028 (2011).
8. A. Taruttis and V. Ntziachristos, "Advances in real-time multispectral optoacoustic imaging and its applications," Nat. Photonics **9**(4), 219–227 (2015).
9. J. Kim, D. Lee, U. Jung, and C. Kim, "Photoacoustic imaging platforms for multimodal imaging," Ultrasonography **34**(2), 88–97 (2015).
10. C. Tian, W. Qian, X. Shao, Z. Xie, X. Cheng, S. Liu, Q. Cheng, B. Liu, and X. Wang, "Plasmonic nanoparticles with quantitatively controlled bioconjugation for photoacoustic imaging of live cancer cells," Adv Sci (Weinh) **3**(12), 1600237 (2016).
11. C. Tian, T. Feng, C. Wang, S. Liu, Q. Cheng, D. E. Oliver, X. Wang, and G. Xu, "Non-Contact Photoacoustic Imaging Using a Commercial Heterodyne Interferometer," IEEE Sens. J. **16**(23), 8381–8388 (2016).

12. K. H. Kim, W. Luo, C. Zhang, C. Tian, L. J. Guo, X. Wang, and X. Fan, "Air-coupled ultrasound detection using capillary-based optical ring resonators," Sci. Rep. **7**(1), 109 (2017).
13. X. Zhu, K. Li, P. Zhang, J. Zhu, J. Zhang, C. Tian, and S. Liu, "Implementation of dispersion-free slow acoustic wave propagation and phase engineering with helical-structured metamaterials," Nat. Commun. **7**, 11731 (2016).
14. S. Zackrisson, S. M. van de Ven, and S. S. Gambhir, "Light in and sound out: emerging translational strategies for photoacoustic imaging," Cancer Res. **74**(4), 979–1004 (2014).
15. C. Tian, Z. Xie, M. L. Fabiilli, and X. Wang, "Imaging and sensing based on dual-pulse nonlinear photoacoustic contrast: a preliminary study on fatty liver," Opt. Lett. **40**(10), 2253–2256 (2015).
16. C. Tian, Z. Xie, M. L. Fabiilli, S. Liu, C. Wang, Q. Cheng, and X. Wang, "Dual-pulse nonlinear photoacoustic technique: a practical investigation," Biomed. Opt. Express **6**(8), 2923–2933 (2015).
17. R. K. Keswani, C. Tian, T. Peryea, G. Girish, X. Wang, and G. R. Rosania, "Repositioning Clofazimine as a Macrophage-Targeting Photoacoustic Contrast Agent," Sci. Rep. **6**(1), 23528 (2016).
18. T. Feng, K. M. Kozloff, C. Tian, J. E. Perosky, Y.-S. Hsiao, S. Du, J. Yuan, C. X. Deng, and X. Wang, "Bone assessment via thermal photo-acoustic measurements," Opt. Lett. **40**(8), 1721–1724 (2015).
19. W. Liu and H. F. Zhang, "Photoacoustic imaging of the eye: a mini review," Photoacoustics **4**(3), 112–123 (2016).
20. A. de la Zerda, Y. M. Paulus, R. Teed, S. Bodapati, Y. Dollberg, B. T. Khuri-Yakub, M. S. Blumenkranz, D. M. Moshfeghi, and S. S. Gambhir, "Photoacoustic ocular imaging," Opt. Lett. **35**(3), 270–272 (2010).
21. S. Hu, B. Rao, K. Maslov, and L. V. Wang, "Label-free photoacoustic ophthalmic angiography," Opt. Lett. **35**(1), 1–3 (2010).
22. S. Jiao, M. Jiang, J. Hu, A. Fawzi, Q. Zhou, K. K. Shung, C. A. Puliafito, and H. F. Zhang, "Photoacoustic ophthalmoscopy for in vivo retinal imaging," Opt. Express **18**(4), 3967–3972 (2010).
23. R. H. Silverman, F. Kong, Y. C. Chen, H. O. Lloyd, H. H. Kim, J. M. Cannata, K. K. Shung, and D. J. Coleman, "High-resolution photoacoustic imaging of ocular tissues," Ultrasound Med. Biol. **36**(5), 733–742 (2010).
24. N. Wu, S. Ye, Q. Ren, and C. Li, "High-resolution dual-modality photoacoustic ocular imaging," Opt. Lett. **39**(8), 2451–2454 (2014).
25. W. Song, Q. Wei, W. Liu, T. Liu, J. Yi, N. Sheibani, A. A. Fawzi, R. A. Linsenmeier, S. Jiao, and H. F. Zhang, "A combined method to quantify the retinal metabolic rate of oxygen using photoacoustic ophthalmoscopy and optical coherence tomography," Sci. Rep. **4**(1), 6525 (2015).
26. S. N. Hennen, W. Xing, Y.-B. Shui, Y. Zhou, J. Kalishman, L. B. Andrews-Kaminsky, M. A. Kass, D. C. Beebe, K. I. Maslov, and L. V. Wang, "Photoacoustic tomography imaging and estimation of oxygen saturation of hemoglobin in ocular tissue of rabbits," Exp. Eye Res. **138**, 153–158 (2015).
27. A. Hughes, "A schematic eye for the rabbit," Vision Res. **12**(1), 123–138 (1972).
28. P. J. Manning, D. H. Ringler, and C. E. Newcomer, *The Biology of the Laboratory Rabbit* (Academic, 1994).
29. L. Ivert, J. Kong, and P. Gouras, "Changes in the choroidal circulation of rabbit following RPE removal," Graefes Arch. Clin. Exp. Ophthalmol. **241**(8), 656–666 (2003).
30. C. H. Chon, X. Y. Yao, R. Dalal, A. Takeuchi, R. Y. Kim, and M. F. Marmor, "An experimental model of retinal pigment epithelial and neurosensory serous detachment," Retina **16**(2), 139–144 (1996).
31. A. Takeuchi, G. Kricorian, X. Y. Yao, J. W. Kenny, and M. F. Marmor, "The rate and source of albumin entry into saline-filled experimental retinal detachments," Invest. Ophthalmol. Vis. Sci. **35**(11), 3792–3798 (1994).
32. A. Negi and M. F. Marmor, "Effects of subretinal and systemic osmolality on the rate of subretinal fluid resorption," Invest. Ophthalmol. Vis. Sci. **25**(5), 616–620 (1984).
33. T. Ma, X. Zhang, C. T. Chiu, R. Chen, K. Kirk Shung, Q. Zhou, and S. Jiao, "Systematic study of high-frequency ultrasonic transducer design for laser-scanning photoacoustic ophthalmoscopy," J. Biomed. Opt. **19**(1), 16015 (2014).
34. Z. Xie, S. Jiao, H. F. Zhang, and C. A. Puliafito, "Laser-scanning optical-resolution photoacoustic microscopy," Opt. Lett. **34**(12), 1771–1773 (2009).
35. Z. Alkin, A. H. Kashani, and M. S. Humayun, "Spectral Domain OCT Measurements of Rabbit Retinal Anatomy," Invest. Ophthalmol. Vis. Sci. **52**, 2682 (2011).
36. A. H. Kashani, E. Kirkman, G. Martin, and M. S. Humayun, "Hyperspectral computed tomographic imaging spectroscopy of vascular oxygen gradients in the rabbit retina in vivo," PLoS One **6**(9), e24482 (2011).
37. Laser Institute of America, *American National Standard for Safe Use of Lasers ANSI Z136.1 - 2007* (American National Standards Institute, Inc., 2007).
38. T. Liu, Q. Wei, W. Song, J. M. Burke, S. Jiao, and H. F. Zhang, "Near-infrared light photoacoustic ophthalmoscopy," Biomed. Opt. Express **3**(4), 792–799 (2012).

## 1. Introduction

Visual impairment and blindness are prevalent worldwide and are increasing in the coming decades due to aging of the population. Eighty percent of the cases are preventable or curable if properly diagnosed and managed [1]. Retinal imaging techniques currently used in the clinic mainly include fundus photography, fluorescein angiography (FA), indocyanine green angiography (ICGA), and optical coherence tomography (OCT) [2]. Fundus photography can capture color fundus images with excellent contrast but only provides structural information.

FA permits visualization of retinal circulation in detail, but its role in studying choroidal circulation is limited due to free permeation of fluorescein in choroidal vessels. Using a larger fluorescence molecule with 98% bound to plasma, ICGA can reveal choroidal circulation but the images are often difficult to interpret. In addition, both FA and ICGA are invasive and require intravenous injection of exogenous dyes that may cause complications such as emesis and anaphylactic reactions [3]. Without the need of dye injection, OCT and OCT angiography can provide structural and functional information of retina, but they often have limited visualization of the choroid and molecular imaging capabilities remain rudimentary [4, 5]. A large clinical need thus remains developing improved chorioretinal imaging techniques.

Photoacoustic imaging is an emerging and noninvasive imaging technology based on energy conversion from light to sound [6–13]. It is being extensively explored in numerous biomedical applications, such as cancer [14], liver [15, 16], rheumatology [17], and bone [18]. In addition to providing structural information, photoacoustic imaging can also reveal functional and molecular details of biological tissue and well suits ophthalmic applications. First emerged in 2010, photoacoustic ocular imaging has been an active field and continues to arouse interests of scientists and clinicians of the optics and ophthalmology communities [19]. de la Zerda *et al.* [20], Hu *et al.* [21], Jiao *et al.* [22], and Silverman *et al.* [23] independently reported photoacoustic imaging of rabbit whole eye *in vivo*, mouse iris *in vivo*, rat retina *in vivo*, and pig eye *ex vivo*, respectively, in 2010. Later, Li and associates investigated photoacoustic and ultrasound dual-modality imaging of different parts of mouse eyes [24]. Song and associates demonstrated photoacoustic and OCT imaging of oxygen metabolic rate of rat retinae [25]. Hennen and associates studied photoacoustic tomographic imaging of oxygen saturation of ciliary body tissues in living rabbits [26].

Most reported work in photoacoustic ocular imaging so far uses mice and rats, the eyeballs of which are small in size (axial length of mouse eyeballs ~3 mm, rats ~6 mm) compared with those of humans (~23 mm). Using animals like rabbits with larger eyeballs may gain more benefits. For example, rabbits have been long used as an animal model in ophthalmic research and possess several advantages over mice and rats. First, rabbit eyes have an axial length of 18.1 mm [27], which is almost 80% of the axial length of human eyes. Second, rabbits have similar physiological changes and vitreous volume to those of humans and have served for many years as an excellent vitreoretinal model [28]. Third, the rabbit choroid is well developed and characterized for studying certain choroidal diseases, such as choroidal neovascularization. Finally, fluid flow across the retinal pigment epithelium (RPE) has been validated in rabbits [29–32]. One downside of rabbit models is that the retinal vasculature is merangiotic rather than holangiotic like mice and humans. These advantages make photoacoustic findings of rabbit models particularly valuable and more clinically translatable.

Despite the significance, developing photoacoustic ocular imaging technologies suitable for high-resolution rabbit eye imaging faces technical challenges. These include ultrasound signal attenuation with distance particularly for high-frequency components, corneal dehydration, and optical aberrations. Since laser spot is tightly focused onto the retina by the eye optics, the intensity of excited photoacoustic signals will experience significant attenuation before being detected. The larger the eyeball size, the more significant is the signal attenuation. The rabbit eyeball axial length of 18.1mm is about three times larger than that of rats and six times larger than that of mice. This poses more challenges for rabbit eye imaging. Based on our previous rabbit whole eye imaging work [20], we developed an integrated photoacoustic microscopy (PAM) and OCT dual-modality imaging platform. Using the system, we have achieved label-free chorioretinal imaging of living rabbits with single-vessel discernible resolution at a safe laser exposure level, which has never been demonstrated before. Since the size of rabbit eyeball is close to that of humans, the work may help clinical translation of the technology.

## 2. Methods

### 2.1 Imaging system

The dual-modality chorioretinal imaging system integrates two cutting-edge modalities: PAM (light path in green color) and spectral-domain OCT (SD-OCT, light path in blue color), as shown in Fig. 1.

In PAM, 570 nm pulsed laser emanating from an optical parametric oscillator (OPO) pumped by a diode-pumped solid-state laser (NT-242, Ekspla, Vilnius, Lithuania, pulse repetition rate 1 kHz, duration 3 – 6 ns, tunable wavelength range 405 – 2600 nm) is first collimated (beam diameter ~3.0 mm), then reflected by a dielectric mirror and a dichroic mirror (DM), and scanned by a galvanometer in two dimensions. After passing through a telescope composed of a telecentric scan lens (focal length 36 mm, OCT-LK3-BB, Thorlabs, Inc., Newton, NJ) and an ophthalmic lens (OL, focal length 10 mm, AC080-010-B-ML, Thorlabs), the scanned laser beam is focused onto the rabbit retina by the eye's optics. Excited photoacoustic signals due to endogenous optical absorption of hemoglobin and melanin are captured by a custom-built needle-shaped ultrasonic transducer (center frequency 27 MHz, two-way −6 dB bandwidth 60%, Optosonic Inc., Arcadia, CA) [33], amplified by a low-noise amplifier (gain 57 dB, AU-1647, L3 Narda-MITEQ, NY), digitized by an analog to digital (A/D) card (PX1500-4, Signatec, Inc., Newport Beach, CA), and finally transferred to a computer. The transducer is placed in contact with the conjunctiva off the central visual axis using a drop of ultrasound gel for signal coupling. No signal averaging is used in data acquisition.

The SD-OCT system was adapted from a commercially acquired OCT system from Thorlabs (Ganymede-II-HR, center wavelength 905 nm, A-line scan rate 36 kHz, scan angle ± 10.6°, beam diameter 5.5 mm) by adding the OL lens after the scan lens and a dispersion compensation glass (DCG) in the reference arm. The OCT light source is a combination of two individual superluminescent diodes, one centered at 846 nm, the other one at 932 nm. The estimated bandwidth is about 220 nm and the theoretical axial resolution in air is calculated to be 1.6 µm. The OCT system shares the same galvanometer, scan lens, and OL with the PAM, and was coaxially aligned to ensure co-registration of the dual-modality images. The OPO laser, digitizer, and the OCT system were synchronized through a DAQ card (USB-6353, National Instruments Corporation, Austin, TX). The OCT system is mainly used to guide PAM and help interpret photoacoustic results by providing anatomy of the retinal layers.
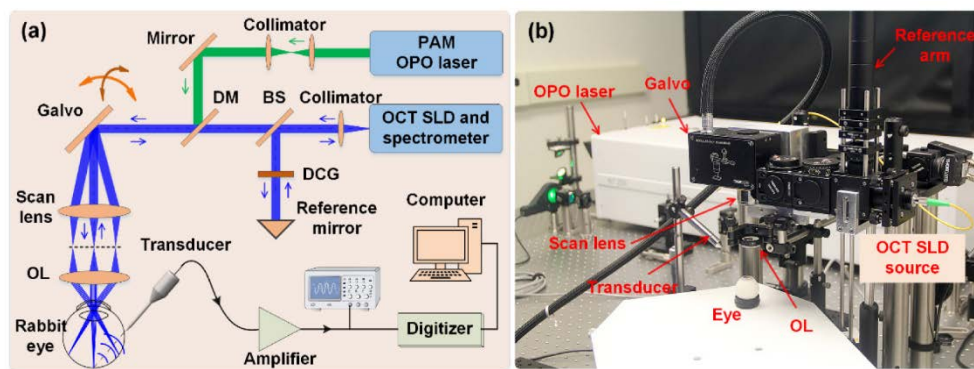


Fig. 1. Integrated photoacoustic microscopy and optical coherence tomography for chorioretinal imaging. (a) Schematic; (b) physical setup. OPO: Optical parametric oscillator; SLD: superluminescent diode; BS: beam splitter; DM: dichroic mirror; DCG: dispersion compensation glass; OL: ophthalmic lens.

## 2.2 Animal experiment

All rabbit experiments were performed in accordance with the ARVO (The Association for Research in Vision and Ophthalmology) Statement for the Use of Animals in Ophthalmic and Vision Research, after approval of the laboratory animal protocol by the Institutional Animal Care and Use Committee (IACUC) of the University of Michigan (Protocol PRO00006486, PI Yannis Paulus).

As a general procedure, rabbits were anesthetized with a mixture of ketamine (40 mg/kg) and xylazine (4 mg/kg) by intramuscular injection. Pupillary dilation was achieved by one drop each of 1% tropicamide and 2.5% phenylephrine hydrochloride. Topical tetracaine 0.5% was instilled in the treated eyes before imaging. After anesthesia and pupil dilation, rabbit fundi were first examined using a fundus camera (TRC 50EX, Topcon Corporation, Tokyo, Japan), and then imaged using the dual-modality system. A water-circulating blanket (TP-700, Stryker Corporation, Kalamazoo, MI) was used to keep the body temperature of the rabbits. During experiments, eyewash (Altaire Pharmaceuticals, Inc., Aquebogue, NY) was applied to rabbit cornea every two minutes to prevent corneal surface keratopathy. Vitals, such as mucous membrane color, heart rate, respiratory rate, and rectal temperature were monitored and recorded every 15 minutes. Post experiment, the rabbit fundi were re-examined using the same Topcon TRC 50EX fundus camera to see any morphological changes of blood vessels due to laser exposure.

## 3. Results and discussion
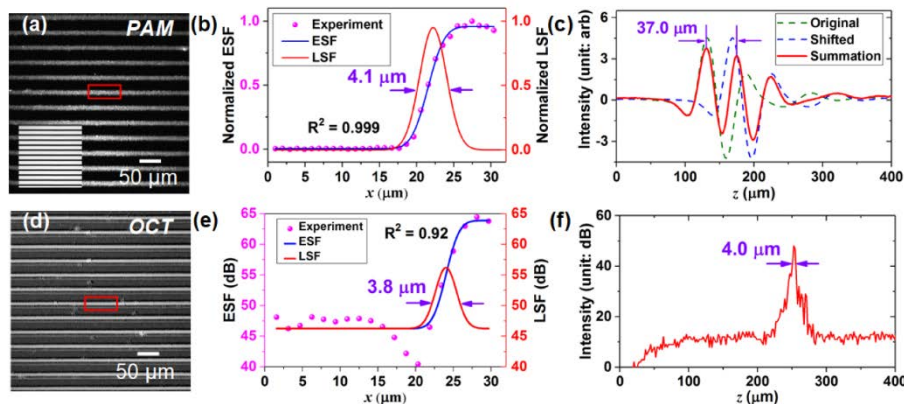
### 3.1 System calibration



Fig. 2. System performance calibration using a chromium grating (linewidth: 10 μm, pitch: 40 μm) coated on a coverslip. (a) PAM image of the grating. Inset is the bright field image. (b) Fitted edge spread function (ESF) and line spread function (LSF) of the experimental data in the rectangular box in (a) show that PAM has a lateral resolution of 4.1 μm. (c) Summation of two A-line axial spread function shows that PAM has an axial resolution of 37.0 μm. (d) OCT image of the grating. (e) Fitted ESF and LSF of the experimental data in the rectangular box in (d) show that OCT has a lateral resolution of 3.8 μm at −6 dB. (f) A-line spread function shows that OCT has an axial resolution of 4.0 μm at −6 dB in air.

Before animal experiments, the performance of the dual-modality imaging system was first calibrated at the focal plane of the scan lens.

A coverslip sample with coated chromium gratings [linewidth: 10 μm, pitch: 40 μm, inset of Fig. 2(a)] providing excellent optical absorption and reflection contrasts as well as sharp edges was used as the target for lateral and axial resolution calibration of PAM and OCT. Figures 2(a) and 2(d) give maximum intensity projections (MIPs) of PAM and OCT C-scans of the grating sample. Using data in the red boxes in Figs. 2(a) and 2(d), edge spread functions [ESFs, Figs. 2(b) and 2(e)] of PAM and OCT were fitted with the Gauss error function; line

spread functions (LSFs) were thus calculated from the ESFs to give lateral resolutions defined by the full-width at half-maximum (FWHM). In this case, the quantified lateral resolutions of PAM and OCT are 4.1 μm and 3.8 μm, respectively. OCT has a better lateral resolution than PAM because its beam diameter (~5.5 mm) is larger than that of PAM (~3.0 mm).

The axial resolution of PAM was calculated by shifting a typical A-line signal (one-dimensional point spread function) and then adding the shifted signal to the original [Fig. 2(c)]. The minimum shift distance that still allows for discrimination of the two peaks according to the FWHM criterion is regarded as the axial resolution [34]. The axial resolution of OCT was simply estimated using the A-line signal width at FWHM [-6 dB, Fig. 2(f)]. In this case, the quantified axial resolutions of PAM and OCT are 37.0 μm and 4.0 μm, respectively.

### 3.2 Chorioretinal imaging in living rabbits

A total of four New Zealand White rabbits (male, ~6 months old, ~3 kg body weight) were used in the imaging experiments [Fig. 3(a)]. Figure 3(b) shows a photograph of a rabbit fundus, which has a horizontal array of retinal vessels rather than having retinal vessels throughout the fundus, such as mice and humans. Two broad white bands of myelinated nerve fibers, the medullary ray, extend nasally and temporally from the optic disk. Retinal blood vessels are confined within this zone and remaining retina is avascular.
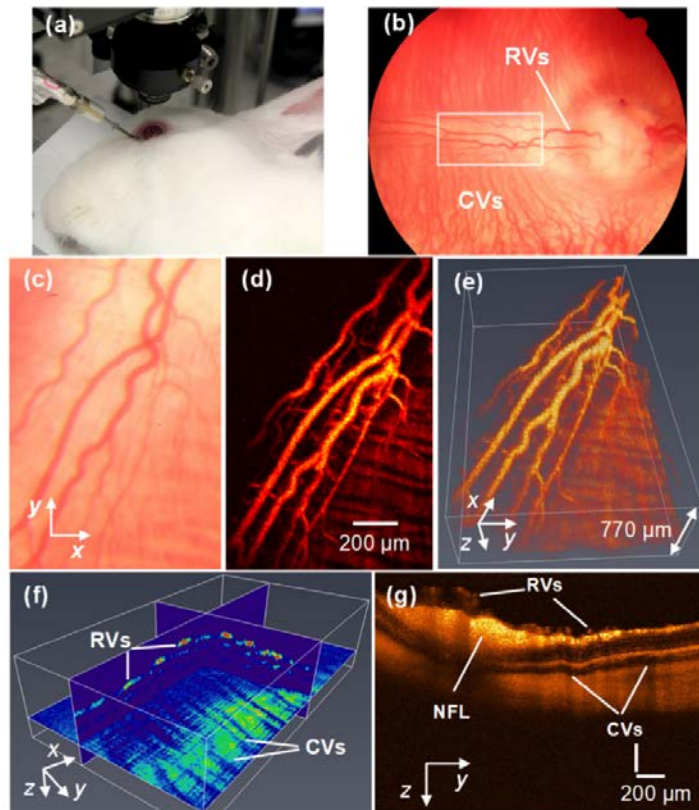


Fig. 3. PAM and OCT dual-modality imaging of retinal blood vessels in rabbits. (a) Experimental photograph showing the rabbit, the ophthalmic lens, and the transducer. (b) Fundus photograph showing rabbit retinal vessels (RVs) originating from the optic nerve are confined in the medullary ray regions. (c) Close-up of the RVs in the white rectangle box in (b). (d) MIP of PAM signals of RVs and choroidal vessels (CVs). (e) 3D volumetric rendering of the PAM image (see Visualization 1). (f) 2D orthogonal slices of the PAM image showing RVs and CVs at different depths. (g) OCT image showing RVs, CVs, NFL, and retinal layers, as demonstrated in [35].

Figure 3(d) shows the MIP of a PAM image of blood vessels within the medullary ray, where single retinal and choroidal vessels are clearly discernible and co-register those in the bright-field image in Fig. 3(c) taken by the fundus camera. Estimated sizes of major retinal vessels range from 70 to 100 μm, which are in good agreement with anatomical data [28]. By incorporating time-of-flight (TOF) information of the photoacoustic signals, three-dimensional (3D) structure of the vessels was reconstructed and rendered (Amira, FEI, Hillsboro, OR), as shown in Fig. 3(e). The retinal and choroidal vessels are well resolved in depth and the shadows of retinal vessels are visible. Figure 3(f) illustrates three orthogonal slices of the volume, showing sections of depth-resolved retinal and choroidal vessels. By retrieving photoacoustic raw data and counting the TOF, the estimated thickness between retinal vessels and choroidal vessels in the medullary ray region is about 200 – 300 μm, which is within the resolving ability (37.0 μm axial resolution) of PAM. The finding also agrees with those in the literature [36] and our OCT images, as shown in Fig. 3(g), in which retinal vessels, choroidal vessels, and the nerve fiber layer (NFL) are easily seen.

In addition to retinal vessels, choroidal vessels in the New Zealand White rabbits were also imaged using the dual-modality system. Figure 4(a) displays a photograph of the rabbit fundus inferior to the optic nerve, showing choroidal vessel distribution. Figure 4(b) shows the MIP of a typical PAM image. The choroidal vessels were delineated with high resolution and single vessels are clearly distinguishable. A similar region was also scanned by OCT. The result, illustrated in Fig. 4(c), confirms the presence of blood vessels in the choroid and reveal different retinal layers.
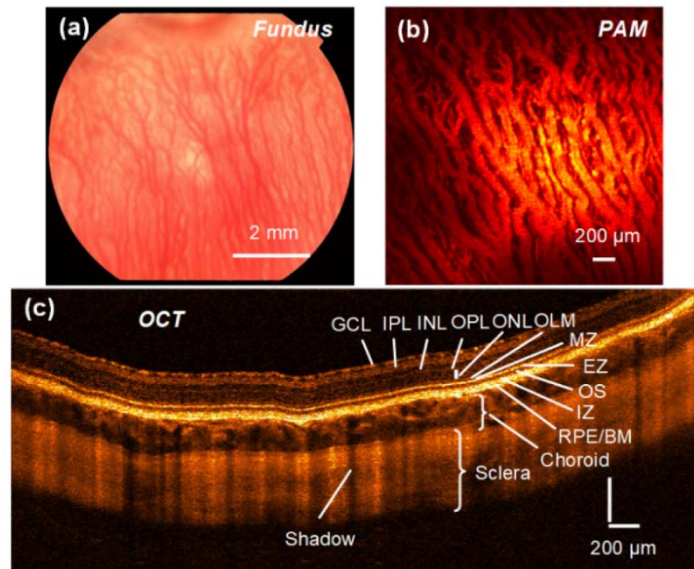


Fig. 4. PAM and OCT dual-modality imaging of choroidal blood vessels in rabbits. (a) Fundus photograph demonstrating the choroidal vessel distribution inferior to the optic nerve. (b) MIP of PAM signals of the CVs. (c) OCT image showing retinal layers, the choroid, and the sclera. GCL: Ganglion cell layer; IPL: inner plexiform layer; INL: inner nuclear layer; OPL: outer plexiform layer; ONL: outer nuclear layer; OLM: outer limiting membrane; MZ: myoid zone; EZ: ellipsoid zone; OS: outer segment; IZ: interdigitation zone; BM, Bruch's membrane.

In the PAM experiments above, the raster-scan regions on the retina have a typical field of view (FOV) of about 3 × 3 mm (limited by the FOV of the ultrasonic transducer) with 256 × 256 pixels. It takes about 65 seconds to finish the data acquisition, limited by the 1 kHz pulse repetition rate of the OPO laser. In the OCT experiments, the B-scan regions on the retina have FOVs up to 6 mm with up to 1024 pixels, which usually takes less than a second due to the 36 kHz A-line scanning rate of the galvanometer.

### 3.3 Ocular light safety

Light safety is an important factor to consider in ocular imaging. In this work, the OCT and PAM light power/energy on rabbit cornea were measured to be ~2.5 mW centered at 905 nm and ~80 nJ at 570 nm, respectively. While the OCT light power exceeds the ANSI safety limit ~1 mW [37] (the OCT system was originally not designed for ocular imaging), the PAM laser energy is below the safety limit.

Several authors have studied photoacoustic laser exposure and concluded that it is possible to achieve photoacoustic ocular imaging with a safe laser exposure dose [21, 22, 38]. In our imaging setup, assuming that the laser spot has a diameter of 20 μm on the retina, the angular subtense of the source

$$\alpha = \frac{20\mu m}{17mm} = 1.2 mrad < \alpha_{min} = 1.5 mrad, \tag{1}$$

where 17 mm is the mean focal length of human eye. This indicates that the laser beam in PAM could be regarded as a point source. ANSI has three different rules to regulate the maximum permissible exposure (MPE) for a point source within the visible band (400 – 700 nm). They are the single pulse limit, the average power limit, and the repetitive pulse limit. For the single pulse limit,

$$MPE_{sp} = 5.0 \times 10^{-7} J / cm^2. \tag{2}$$

For the average power limit, since the total laser exposure time is about 65 s, the total $MPE_{total}$ = $6.5 \times 10^{-2} J/cm^2$. Within a laser spot of 20 μm, there are at most two overlapping laser pulses ($n_{total}$ = 2). The MPE per pulse

$$MPE_{total} / n_{total} = 3.3 \times 10^{-2} J / cm^2. \tag{3}$$

For the repetitive pulse limit,

$$MPE_{rp} = n_{Total}^{-0.25} MPE_{sp} = 4.2 \times 10^{-7} J / cm^2. \tag{4}$$

Among the three, the repetitive pulse limit is the most conservative. Considering that a dilated human pupil have a typical diameter of $D$ = 7 mm [22], the maximum permissible single laser pulse energy on the retina is

$$E = MPE_{rp} \times \pi \times \left(\frac{D}{2}\right)^2 = 160 nJ. \tag{5}$$

The calculated ANSI safety limit 160 nJ is the strictest compared with the values 200 nJ (point source) reported in [22] and 1.3 μJ (extended source) in [21]. Apparently, the laser pulse energy ~80 nJ used in the experiment is below this safety limit. Considering that the PAM images (Fig. 3 and Fig. 4) have good signal-to-noise ratios and transducer array could potentially be used to replace the single point transducer, we still have adequate room to further reduce the laser energy. In addition, the above safety limit only applies to visible band light. When imaging with laser wavelengths in the near-infrared region mediated with contrast agents, the laser exposure limit would be elevated.

## 4. Discussion and conclusions

PAM is a new eye imaging modality based on optical absorption contrast of biological tissue. It is sensitive to endogenous and exogenous absorbers, like hemoglobin, melanin, and externally-administered contrast agents. Looking at blood vessel structures based on light absorption of hemoglobin is a basic application of PAM. Its more broad advantages are in functional and molecular imaging aspects. That is to say, PAM can detect blood flow,

hemoglobin concentration, oxygen saturation, and biomarkers and suits well the study of pathophysiology of some ocular diseases. In addition, the depth penetration of PAM imaging is greater than that of OCT. OCT is based on the scattering contrast of tissue while OCT angiography is based on scattering contrast of tissue and motion contrast of red blood cells. OCT angiography is becoming popular in clinic to image eye blood vessels and detect blood flow, but its molecular imaging capability is limited due to its contrast mechanism. From this perspective, PAM might provide useful information that will supplement the information provided by OCT and OCT angiography.

In conclusion, we have developed a combined dual-modality system for chorioretinal imaging in rabbits including PAM and OCT. The system has excellent performance (PAM and OCT lateral resolution 4.1 μm and 3.8 μm, axial resolution 37.0 μm and 4.0 μm, respectively) and could achieve label-free vascular imaging by leveraging endogenous optical absorption and scattering contrast of ocular tissue. Experimental results in rabbits demonstrate that the PAM could noninvasively resolve retinal and choroidal blood vessels at single-vessel discernible resolution using a laser exposure dose (~80 nJ) below the ANSI safety limit (160 nJ) at 570 nm; and the OCT could finely distinguish different retinal layers, the choroid, and the sclera. Since rabbits have a closer eyeball size to that of humans, the presented work may have a major impact on clinical translation of photoacoustic microscopy of the eye.

## Funding

## Acknowledgments